

Microstructural Evolution of Graded Transition Joints



JONATHAN P. GALLER, JOHN N. DUPONT, SUDARSANAM SURESH BABU,
and MOHAN SUBRAMANIAN

Carbon diffusion and the associated microstructural changes in dissimilar metal welds at elevated temperatures lead to a microstructure that is susceptible to premature failure. Graded transition joints (GTJs) can potentially provide a viable replacement to prolong the service life of these components. The purpose of the current investigation is to fabricate, age, and characterize GTJs using three candidate filler metals (Inconel 82, EPRI P87, and 347H) to understand the microstructural evolution at elevated temperatures. Microhardness measurements were performed on the GTJs in the as-welded and aged conditions to understand the initial strength gradients throughout the graded region and how they evolve with aging time. Additionally, energy dispersive spectrometry was performed to measure the compositional gradients, which were input into thermodynamic and kinetic calculations to understand the carbon diffusion behavior and phase stability. Enhanced carbon diffusion occurred at the layer interfaces in the graded region of the GTJ, which indicated important regions that undergo microstructural evolution. The hardness results also revealed hardness changes at the layer interfaces. The analyzed interfaces demonstrated that carbon diffusion and corresponding carbide redistribution occurred that accounted for the observed hardness gradients. Additionally, the transition from a martensitic to austenitic region was observed in each GTJ that contributed to the hardness variations in the graded region. Finally, the formation of a nickel-rich martensitic constituent was observed in the graded region of all filler metals after aging. This constituent was originally austenite at the aging temperature, and transformed to martensite with no change in composition upon cooling. The morphologies of the constituent in the three filler metals are presented and discussed.

<https://doi.org/10.1007/s11661-019-05138-8>

© The Minerals, Metals & Materials Society and ASM International 2019

I. INTRODUCTION

DISSIMILAR metal welds (DMWs) are critical for design, development, and manufacturing of very high temperature reactors, specifically steam generators in the nuclear industry. Several joining techniques can be used to join dissimilar material combinations such as diffusion bonding, arc welding, and laser beam welding.^[1–3] Experience has demonstrated that failures of such DMWs can be caused by strain localization attributed to carbon diffusion and thermal stresses due to the chemical potential of carbon (CPC) gradient and the coefficient of thermal expansion (CTE) and mechanical property mismatch.^[4,5] Each of these factors is caused by the large variation in composition across the

narrow interface between the two dissimilar materials. These failures can occur well before the expected service lifetime, and can cost power plants up to \$850,000 per day in lost revenue and repair costs.^[6] A potential solution to DMW failures is the design and implementation of graded transition joints (GTJs).

Functionally graded materials have been considered for use in components exposed to high temperature gradients.^[7] A typical functionally graded material consists of a ceramic–metal mixture that can be tailored to utilize the advantages of the individual material properties. The ceramic part has good thermal and corrosion resistance capabilities, and the metallic part provides superior fracture toughness and ductility.^[8,9] A GTJ is a type of a fully metallic functionally graded material that consists of two regions of “pure” material on either side of a region where the two materials are mixed in continuously varying proportions over a known distance. This region has a graded composition that is significantly longer than what is reported in DMWs, by as much as three orders of magnitude.^[4,10,11] By continuously grading the composition, the sharp changes in both composition and material properties within DMWs are broadened over the length of the

JONATHAN P. GALLER and JOHN N. DUPONT are with Lehigh University, 5 East Packer Ave., Bethlehem PA, 18015. Contact e-mail: Jonathan.Galler@pw.utc.com SUDARSANAM SURESH BABU and MOHAN SUBRAMANIAN are with the University of Tennessee, Knoxville, 1512 Middle Drive, Knoxville TN, 37996.

Manuscript submitted June 5, 2018.

Article published online March 6, 2019

grade to mitigate many of the factors that cause premature failure.^[12] In the context of the power generation industry, useful GTJs can be fabricated by multipass welding or additive manufacturing processes.

While GTJs present a potentially viable solution to the problems associated with DMWs, the complex microstructural and property gradients introduce challenges to their effective design and implementation. Design of GTJs using finite element analysis (FEA) tools can potentially expedite the process, provided that the inputs to the model are of sufficient quality so as to produce meaningful outputs. Recent studies have investigated the modeling of functionally graded materials using predictive finite element modeling incorporating ‘effective’ material properties.^[5,7,8] These effective properties are typically estimated using numerical methods such as a simple rule of mixtures, as shown in Eq. [1]:

$$P_{\text{eff}} = fP_A + (1 - f)P_B, \quad [1]$$

where P_{eff} is the effective property, f is the volume fraction of material A, and P_A and P_B are the properties of material A and B, respectively. Young’s modulus, CTE, and Poisson’s ratio are examples of thermal and mechanical properties that are typically estimated in this manner. This technique requires obtaining only the properties for the two materials, rather than measuring properties at a given location in the graded region. FEA tools such as ANSYS can be used for modeling external forces and thermal behaviors the materials are likely to experience, thus the effectiveness of the graded material in service can be determined.

Even though the properties of the graded region can potentially be estimated with such techniques, experimental information is still needed to validate these models. Furthermore, it would be very difficult to estimate how the properties change during aging. One of the important requirements of a GTJ is the stability of the microstructure and properties at an elevated temperature during the service life of the component. It is therefore essential to understand the microstructural evolution of GTJs during long-term exposure.

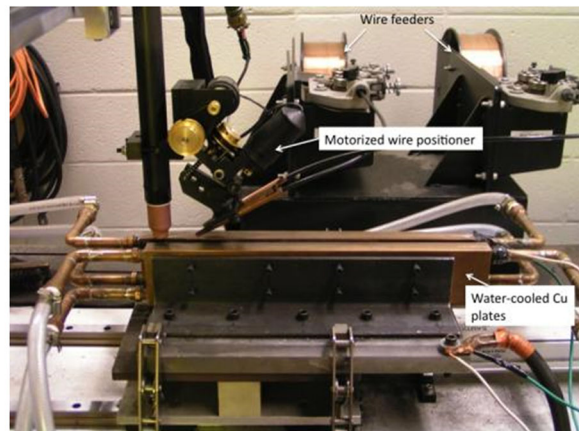
Brentrup and DuPont^[13] modeled the carbon diffusion of a DMW and GTJ between Grade 22 and Alloy 800H. A longer grade length significantly reduced the concentration gradient and associated CPC gradient and thus, reduced the extent of carbon diffusion. Transition joints were also fabricated by Sridharan *et al.*^[14] using a blown powder additive manufacturing process to join Grade 22 to 316 L with SS410 filler. That study attempted to reduce solidification cracking susceptibility of Inconel 82 during fabrication by grading 316L with an intermediate filler metal (SS410). Although they successfully fabricated and characterized a GTJ in the as-welded condition, there is still a need to understand the carbon migration and concomitant microstructural evolution that occurs during aging at high temperatures.

While there is a large body of work on the characterization of DMWs, it is unknown how GTJs will respond to elevated temperatures, and whether it is a suitable replacement for DMWs. The present paper

aims to understand the microstructural evolution and localized hardness changes that occur during fabrication and aging of GTJs made between Grade 22 steel and three candidate filler metals (Inconel 82, EPRI P87, and 347H). Microhardness measurements were performed on the GTJs in the as-welded and aged conditions to understand the initial strength gradients throughout the graded region and how they evolve with aging time. Additionally, energy dispersive spectrometry was performed to measure the compositional gradients, which were input into thermodynamic and kinetic calculations to understand the carbon diffusion behavior and phase stability. The results of this work demonstrate the reduced carbon diffusion and resistance to adverse microstructure changes of GTJs relative to conventional DMWs, and provide a basis for continued improvement to the design and fabrication of GTJs.

II. EXPERIMENTAL PROCEDURE

A conventional DMW was fabricated between Grade 22 and Alloy 800H using Inconel 82 filler metal. The gas tungsten arc welding (GTAW) process was used with a single V-Joint configuration. This provided a baseline comparison to the fabricated GTJs. The GTJ fabrication processes utilized a dual-wire GTAW system equipped with two copper cooling plates to contain the liquid weld pool. A substrate of Grade 22 plate 3” × 12” × ½” (0.076 × 0.305 × 0.013 m) was placed between two copper cooling plates so that the torch and wire feeder assembly deposited metal on the ½” (0.013 m) surface for a maximum travel distance of 12” (0.305 m). The fabrication setup is shown in Figure 1(a). The



(a)



(b)

Fig. 1—(a) Image of the GTJ fabrication set up and (b) schematic representation of the final GTJ product.

feed rates of each filler metal were varied with every deposited layer to meet the required dilution for each layer, and the desired dilution values were calculated from previous modeling studies.^[15] Ten layers were deposited using a current of 250 A, voltage of 12.5 V, and travel speed of 1 mm/s. These parameters were chosen from a wide range of initial parameters because they provided defect-free welds with good control of the weld metal dilution. The welding direction was rotated every two passes to avoid weld metal build up at the end members. The ten layers corresponded to ~ 10 mm graded region, as it was previously determined each layer was ~ 1 mm under the current welding conditions. The wire feed rates combined for a maximum of 50 in/min (21.167 mm/s). Additional three layers of filler metal were deposited so the graded region avoided affects from the joining of 800H extensions. The final product was a three-inch substrate of Grade 22, ~ 10 mm graded region, and a three-inch 800H extension joined using Inconel 82 filler metal, as shown in Figure 1(b). The three filler metals used to fabricate the three GTJs were Inconel 82, P87, and 347H. These candidate filler metals were selected from a wide range of austenitic alloys for several reasons. First, all the alloys are approved by the pertinent codes for use in high temperature service and would therefore not require extensive testing prior to full scale use. Second, the alloys have already been used extensively for joining ferritic and austenitic alloys and are known to exhibit good high temperature strength. Lastly, a separate modeling study was conducted^[16] in which the difference in carbon chemical potential between Grade 22 and a wide range of austenitic filler metals was calculated, and these alloys exhibited the smallest difference in CPC relative to Grade 22. The compositions of the materials used in this study can be seen in Table I.

Samples from the as-welded conventional DMW and GTJs were sectioned and prepared using standard metallographic techniques to a final polished state using 0.05 μm colloidal silica for characterization. Compositional line traces using energy dispersive spectrometry (EDS) were conducted on the as-fabricated GTJ samples in the as-polished condition using the Leo Gemini® 1550 VP scanning electron microscope equipped with an 80 mm² Oxford® X-MAX silicon drift detector operated at an operating voltage of 15 keV with a 60 μm objective aperture. The remaining weld sections were

aged at 600 °C up to 8000 hours (approximately one year) for an accelerated aging treatment to simulate the microstructural evolution expected from service conditions. Samples were removed after 2000, 4000, and 8000 hours and were prepared for characterization similar to the as-welded samples.

Hardness traces were conducted on the as-welded and aged samples in the as-polished condition using a LECO® LM 248AT Vickers microhardness indenter with a 13-second dwell time with 5 and 10 g loads for DMWs and GTJs, respectively. The indenter was calibrated using standard calibration blocks, and approximately five to twenty indents were placed in each GTJ layer to improve the statistical significance of the data. A two percent nital solution was used to reveal grain boundaries and carbides in the ferritic material, and a ten percent oxalic acid solution was used to reveal grain boundaries and carbides in the austenitic structures by electrolytic etching at 2 V for 5 to 15 seconds, depending on filler metal.

Secondary electron imaging and X-ray EDS were performed in a Hitachi® 4300SE/N Schottky field emission scanning electron microscope at an operating voltage of 15 keV. Compositions measured from this analysis are standardless and therefore, semi-quantitative. However, the accuracy of this technique was evaluated using commercial alloy “standards” of known chemistry measured by optical emission spectroscopy (OES). Table II shows the results from EDS alongside the OES results. The EDS measurements show reasonably good agreement with the OES measurements. Therefore, this measurement technique was sufficient enough to identify regions of local enrichment. Monte Carlo simulations using the CASINO® program demonstrated that the X-ray generation volume was approximately 1 μm^3 under the operating conditions.^[17] Thus, results of sub-micron size particles were likely affected by the surrounding matrix material but were still useful for identifying the formation of expected phases. Electron back scattered diffraction (EBSD) measurements were performed at an accelerating voltage of 20 keV and a step size of 0.2 microns across the welded interfaces. Image quality and phase maps were recorded to aid in microstructure characterization.

Thermodynamic and kinetic modeling was conducted on the conventional DMW and the three GTJs. Simulated aging times and temperatures were selected to

Table I. Chemical Compositions of the Grade 22 Plate and Four Welding Wires, and Inputs to the Thermodynamic and Kinetic Models

Material	Elements (All Values in Weight Percent)												
	Al	C	Cr	Cu	Mn	Mo	Nb	Ni	P	S	Si	Ti	Fe
Grade 22 Substrate	0.03	0.07	2.20	0.14	0.52	0.92	< 0.01	0.10	0.007	0.009	0.20	< 0.01	bal.
Inconel 82	—	0.027	21.4	0.016	3.20	—	2.36	70.8	0.003	< 0.001	0.19	0.43	bal.
EPRI P87	0.18	0.11	8.99	—	1.53	1.93	1.08	bal.	0.004	0.001	0.22	0.10	40.4
347H	—	0.05	19.4	0.15	1.75	0.29	0.68	9.07	0.02	0.01	0.44	—	bal.
90S-B3 (Grade 22 Wire)	0.01	0.07	2.45	0.16	0.60	0.93	< 0.01	0.13	< 0.005	0.005	0.58	—	bal.

match the accelerated aging treatment at 600 °C. Aging simulations were performed using the DICTRA® software package in conjunction with the MOB2 mobility database.^[18,19] The TCFE7 and NI-DATA-V7 databases were used for high iron materials and nickel-based alloys, respectively.^[20,21] The following phases were allowed to form based on relevant literature for each material: Austenite, ferrite, $M_{23}C_6$, M_6C , and FCC2 (MC carbide phase).^[22–25] The length of the graded region was set as 50 μm for DMW calculations. This is a typical distance of the PMZ in a DWM.^[4,10,11,26] Composition profiles for the GTJs were chosen from the EDS line trace results utilizing a step function concentration gradient, with individual layer compositions averaged from experimental measurements. Carbon diffusion and phase fraction profiles were extracted from the kinetic simulations for both the DMW and GTJ and were compared to the observations from characterized samples. Additionally, non-equilibrium (Scheil) solidification calculations were performed for compositions representative of select regions of the GTJs using Thermo-Calc software and the TTNi7 thermodynamic database to assess the compositional gradients during weld metal solidification. EDS line scans were acquired across the cellular substructure in the as-welded condition to directly compare to the Scheil simulations.

III. RESULTS

A. Microhardness Trends

1. As-welded condition

Microhardness gradients in the as-welded condition for the conventional DMW and fabricated GTJs using Inconel 82, P87, and 347H are shown in Figure 2(a) through (d), respectively. The microhardness and composition are plotted as a function of distance across the PMZ in the DMW, and graded region in the GTJ. Due to the difficulties of accurately measuring carbon, the carbon concentration gradient was estimated from knowledge of the concentration of major elements (measured by EDS) in the manner previously described by Kusko and DuPont.^[27] Using the measured values of manganese (Mn), nickel (Ni), chromium (Cr), and molybdenum (Mo), along with estimated values of carbon (C), the variation in martensite start (M_s) temperature across the PMZ and graded regions was also determined and shown in Figure 2. The size of the martensite band in the PMZ is controlled by the magnitude of concentration gradient (including C), and previous work^[24] has shown that this technique provides a good estimate of the size of the martensite band in the partially mixed zone, thus providing justification for the approach. This is useful to determine the region where the M_s temperature is below room temperature (T_{RM}), which indicated the material will be austenitic. The expression used for this calculation was provided by Andrews^[28] and is shown in Eq. [2]:

$$M_s(^{\circ}\text{C}) = 539 - 423C - 30.4\text{Mn} - 17.7\text{Ni} - 12.1\text{Cr} - 7.5\text{Mo}, \quad [2]$$

where the composition is in weight percent. The conventional DMW (Figure 2(a)) shows a steep concentration gradient for the three major alloying elements Fe, Ni, and Cr. As expected, the M_s temperature also exhibits a steep gradient across the narrow PMZ. There is a high hardness region in the heat-affected zone (HAZ) of Grade 22 prior to the fusion line, with a significant reduction in hardness from 400 to 200 HV across the PMZ and into the Inconel 82 weld metal.

The spatial variation in composition, hardness, and M_s temperature are shown for Grade 22/Inconel 82 GTJ in Figure 2(b). The difference in length scales between Figure 2(a) and (b) should be noted, as the PMZ of the DMW is on the order of microns, whereas the graded region of the GTJ is on the order of millimeters. The primary goal of GTJs is to eliminate the sharp gradients in composition and associated properties. Although the GTJs do exhibit changes in hardness, these changes occur over much greater distances when compared to the conventional DMW. The composition changes gradually throughout the graded region, and is in the form of a “step function,” as each layer consists of a constant composition. The base metal hardness starts around 200 HV, and increases throughout the HAZ and into the graded region. The hardness increases throughout the graded region and then decreases slightly in Layer 4. Layer 4 exhibits a larger reduction in hardness from 400 to 200 HV. (Note: layers will be labeled “L” followed by the layer number. *i.e.*, layer 1 is L1.) Beyond L4, the hardness remains essentially constant until the end of the graded region, and experiences a slight increase as it transitions to the Inconel 82 weld metal.

The P87 and 347H GTJs (Figures 2(c) and (d)) follow similar trends to that of Inconel 82. The region of mixed hardness in the P87 GTJ is L6 (opposed to L4 in Inconel 82) and in L10 for the 347H GTJ. Furthermore, the concentration gradient is less severe in the 347H GTJ than the other two filler metals because 347H is an iron-base filler metal, whereas Inconel 82 and P87 are nickel-base materials.

2. Aged condition

The microhardness gradients in the aged conditions for the conventional DMW and GTJs are shown in Figures 3(a) through (d). The conventional DMW in Figure 3(a) is relatively soft prior to the fusion line for the aged conditions, and the hardness peaks in the Inconel 82 weld metal. This can be directly compared to the microhardness gradients shown in Figure 3(b) for the Inconel 82 GTJ. The Inconel 82 GTJ also exhibits a reduction in hardness in the HAZ from the as-welded condition, but the extent of softening near the HAZ/L1 interface is significantly reduced. For all aged conditions, there is an overall decrease in hardness relative to the as-welded condition in the Grade 22 region, followed by an increase in hardness in the first several layers of the graded

Table II. Average EDS Measurements Compared to OES Results for the Custom Standards

Standards		Elements (Values Given in Wt Pct. N/A = Not Measured)								
		Si	Cr	Mn	Fe	Co	Ni	Cu	Nb	Mo
Alloy 800	Ave	0.33	22.4	0.95	44.6	0.21	31.9	0.15	N/A	0.42
	OES	0.44	20.9	1.03	41.1	0.07	34.7	0.27	0.15	0.16
347	Ave	0.72	18.2	1.81	67.8	0.29	9.51	0.38	0.76	0.53
	OES	0.55	17.4	1.67	69.9	N/A	9.60	0.47	N/A	0.34
T22	Ave	0.49	2.37	0.57	94.8	0.21	0.07	0.03	N/A	1.41
	OES	0.38	2.19	0.50	bal.	N/A	0.06	0.09	N/A	1.01

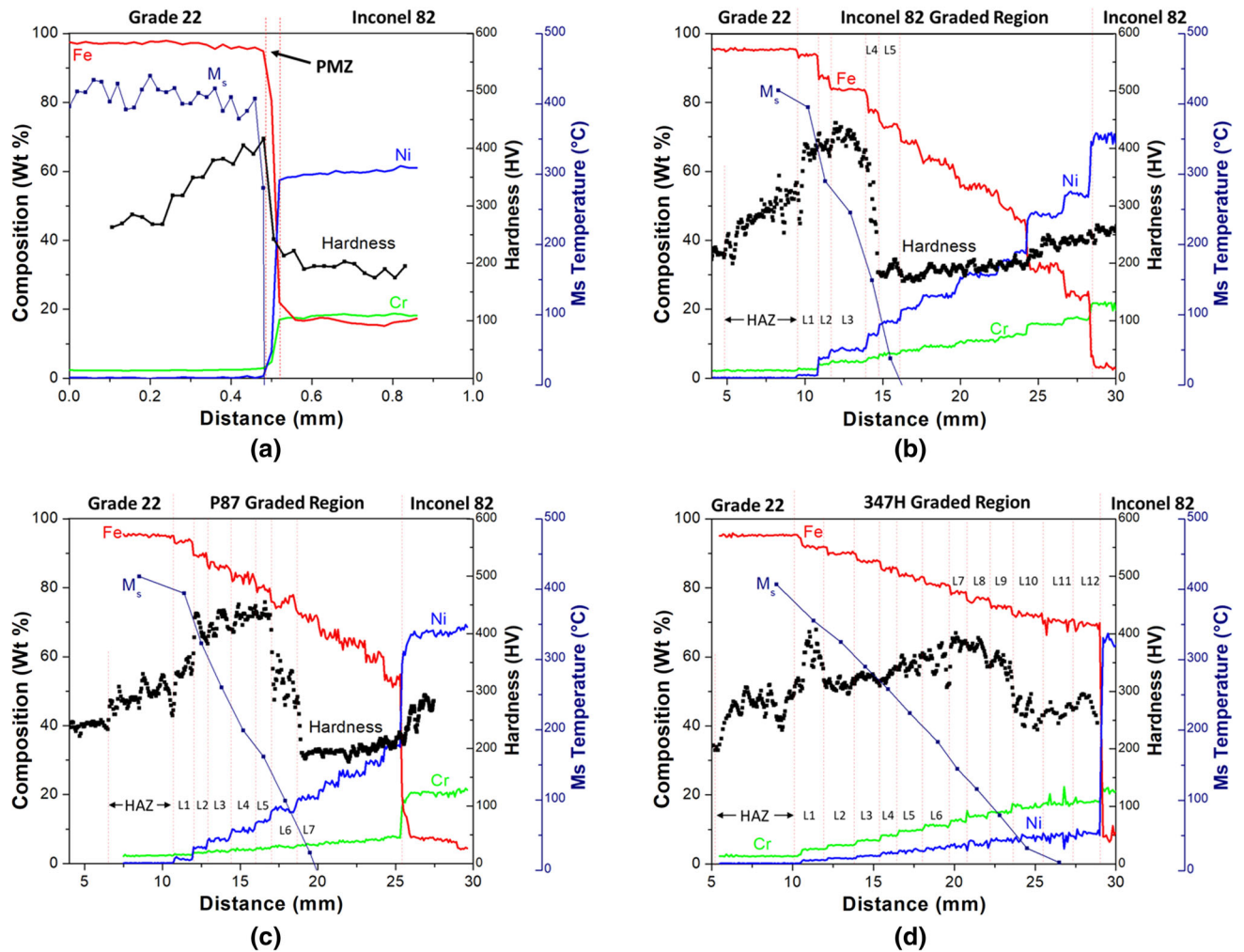


Fig. 2—Composition, hardness, and martensite start temperature as a function of distance for (a) DMW and GTJs between Grade 22 and (b) Inconel 82, (c) P87, and (d) 347H.

region. Layer 5 contains mixed hardness, followed by a reduction slightly below ~ 200 HV in the remaining graded region for the 2000- and 4000-hour aged conditions. After aging for 8000 hours, the hardness is higher (in L6 through the Inconel 82 weld metal) than the 2000-hour aged condition. Similar trends are shown in the P87 GTJ (Figure 3(c)), except the hardness does not increase after

8,000 hours aging, and the mixed hardness layer is L6 (opposed to L5 in the Inconel 82 GTJ). The 347H GTJ (Figure 3(d)) also exhibits similar hardness trends, only over a larger region, and does not exhibit the sharp decrease in hardness like Inconel 82 and P87 in L6 and L7, respectively. Instead, the reduction in hardness occurs beyond L10 (~ $x = 25$ mm), and increases after aging.

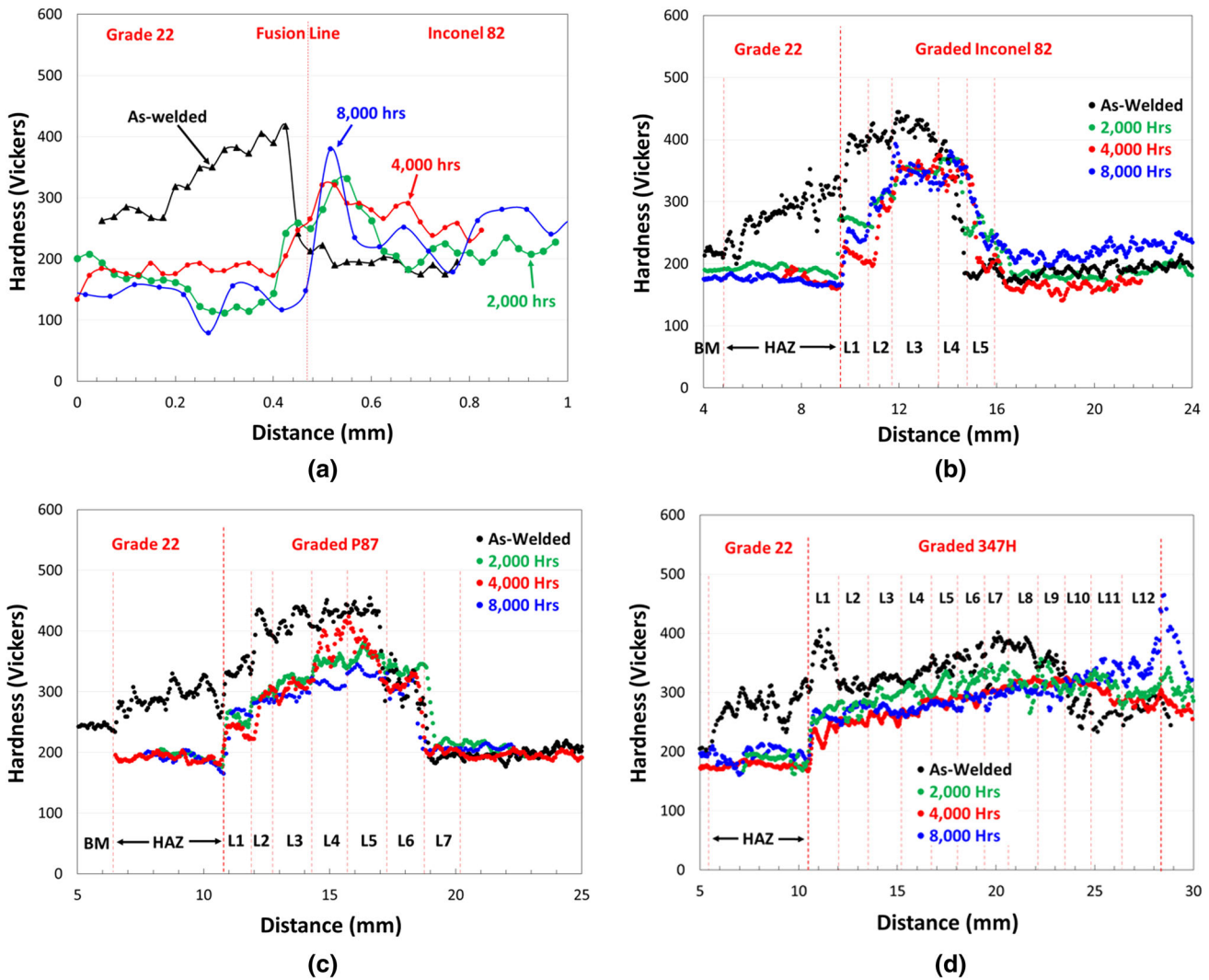


Fig. 3—Hardness as a function of distance for (a) DMW and GTJs between Grade 22 and (b) Inconel 82, (c) P87, and (d) 347H for the as-welded and aged conditions.

B. Thermodynamic and Kinetic Modeling

The calculated carbon concentration and phase fraction as a function of distance at the simulated aging temperature of 600 °C for up to 8000 hours are shown for the conventional DMW (Figure 4(a) and (b)) and the Inconel 82 GTJ (Figures 4(c) and (d)), respectively. (Note the large difference in both concentration and distance scales between the DMW and GTJ.) The conventional DMW shows a carbon-depleted region prior to the fusion line ($x = 10$ mm) and a carbon-enriched region in the PMZ for all aging conditions. The phase fraction at 600 °C in Figure 4(b) shows three stable carbides, a molybdenum-rich carbide (M_6C), chromium-rich carbide ($M_{23}C_6$), and niobium-rich carbide (NbC). The NbC is stable in Inconel 82 due to the higher Nb content in the filler metal. There is a rather sharp transition from BCC to FCC, which is attributed to the steep concentration gradients between the two materials. These figures can be directly compared to the GTJ between Grade 22 and Inconel 82 showing the carbon concentration and phase fraction in Figures 4(c)

and (d), respectively. The initial carbon concentration profile (Figure 4(c)) exhibits a slight, local reduction at the interfaces associated with the change in composition of each layer. After 8000 hours, the extent of carbon depletion and enrichment increases at the first four layer interfaces. This is insightful, as it demonstrates the location of significant microstructural evolution—in the beginning of the grade, and at the layer interfaces. While carbon diffusion occurs in the GTJ, the extent of the enriched regions is less than 0.17 wt pct C, as opposed to 0.70 wt pct C in the DMW PMZ. This is expected, as an increase in grade length and corresponding decrease in the CPC gradient (discussed below) results in a lower driving force for carbon diffusion.

Localized variations in the BCC and FCC phase distribution occur through the first five layers of the graded region (Figure 4(d)). The $M_{23}C_6$ carbide fraction follows the trend of the carbon concentration. This is expected, as it was previously demonstrated that most of the carbon in the system resides primarily in the carbides.^[16] Similar to the DMW, the Nb carbide is

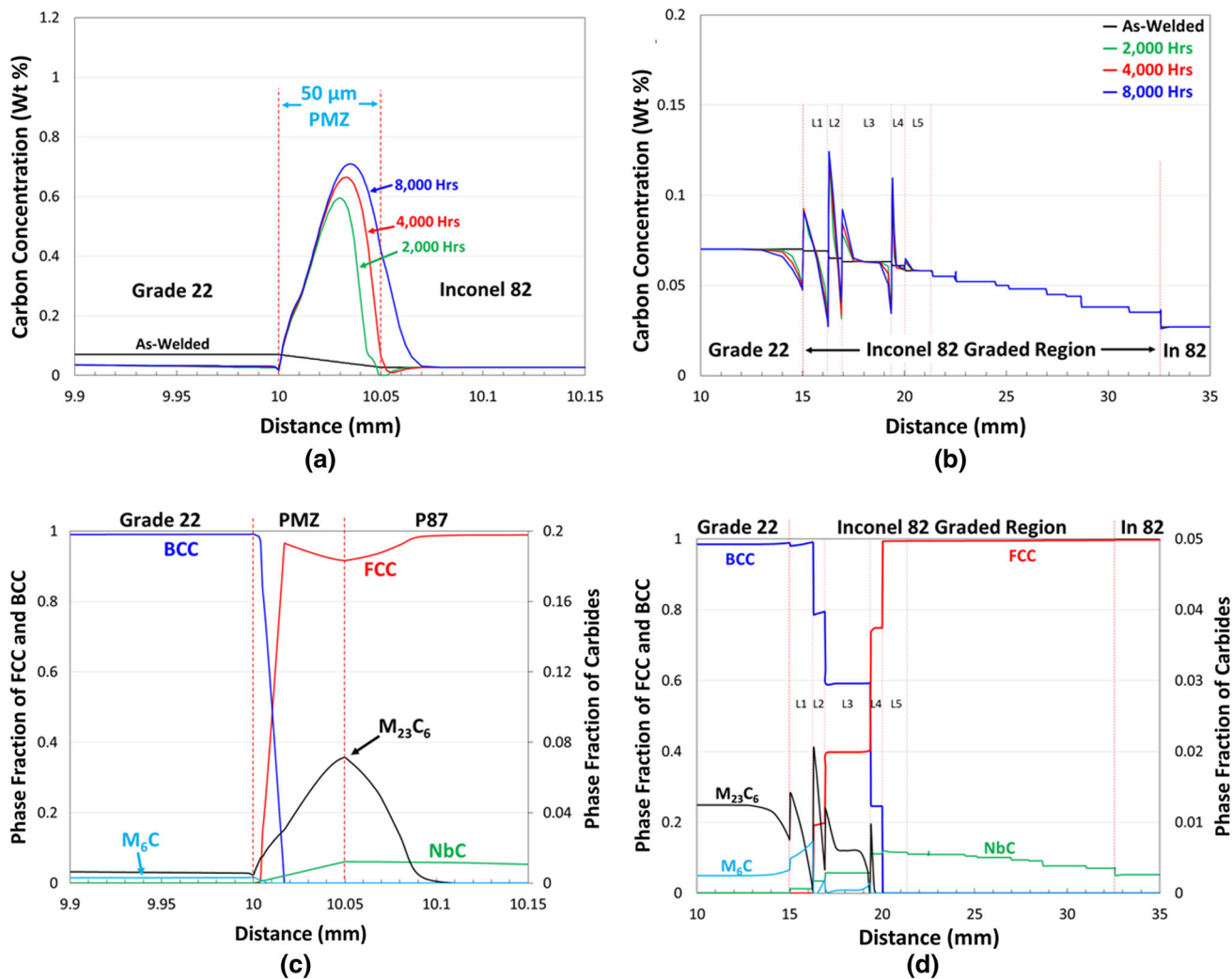


Fig. 4—Calculated carbon concentration and phase fraction as a function of distance at the simulated aging temperature of 600 °C for 8000 h for (a, b) conventional DMW and (c, d) the Inconel 82 GTJ.

stable throughout the FCC range until the end of the graded region and also follows the carbon concentration behavior once the $M_{23}C_6$ carbide is no longer stable.

The carbon concentration and phase fraction as a function of distance are shown for the P87 GTJ (Figures 5(a) and (b)) and the 347H GTJ (Figures 5(c) and (d)), respectively. Similar trends are observed for these GTJs. Carbon diffusion occurs at the layer interfaces, and the extent of diffusion increases with increased aging time. A major difference between these filler metals and Inconel 82 is that the carbon depletion and enrichment at the layer interfaces continues further into the graded region (Figures 5(a) and (c)). The phase fraction for P87 GTJ (Figure 5(b)) shows that all three carbides are stable throughout the graded region. The phase fraction for the 347H GTJ shows a gradual transition (in the form of a step function) from BCC to FCC, attributed to the lower concentration gradient as compared to the Ni-base filler metals. Additionally, the $M_{23}C_6$ phase fraction shows significant depletion and enrichment at the layer interfaces, with NbC stable throughout the entire 347H graded region.

The carbon concentration is lower in Grade 22 than in P87, resulting in a positive concentration gradient in the P87 graded region (Figure 5(a)). In a binary system, carbon will diffuse from high to low concentrations.^[29,30] However, in a multicomponent system, the CPC gradient is the driving force for carbon diffusion. The CPC gradient is shown in the as-welded and aged conditions for the conventional DMW, Inconel 82, P87, and 347H GTJs in Figures 6(a) through (d), respectively. In the as-welded condition, the conventional DMW has a steep CPC gradient after the fusion line that drives the carbon to diffuse from Grade 22, down the CPC gradient, and into the PMZ. In the aged condition, the CPC discontinuity that existed at the fusion line in the as-welded condition is alleviated due to carbon diffusion. The three GTJs show a step function in the negative CPC gradient for all conditions. Even though the P87 GTJ has a positive carbon concentration gradient, it exhibits a negative CPC gradient across the graded region, as shown in Figure 6(c). This results in carbon to diffuse up the concentration gradient, a phenomenon known as “uphill” diffusion.^[10,11,29,31,32]

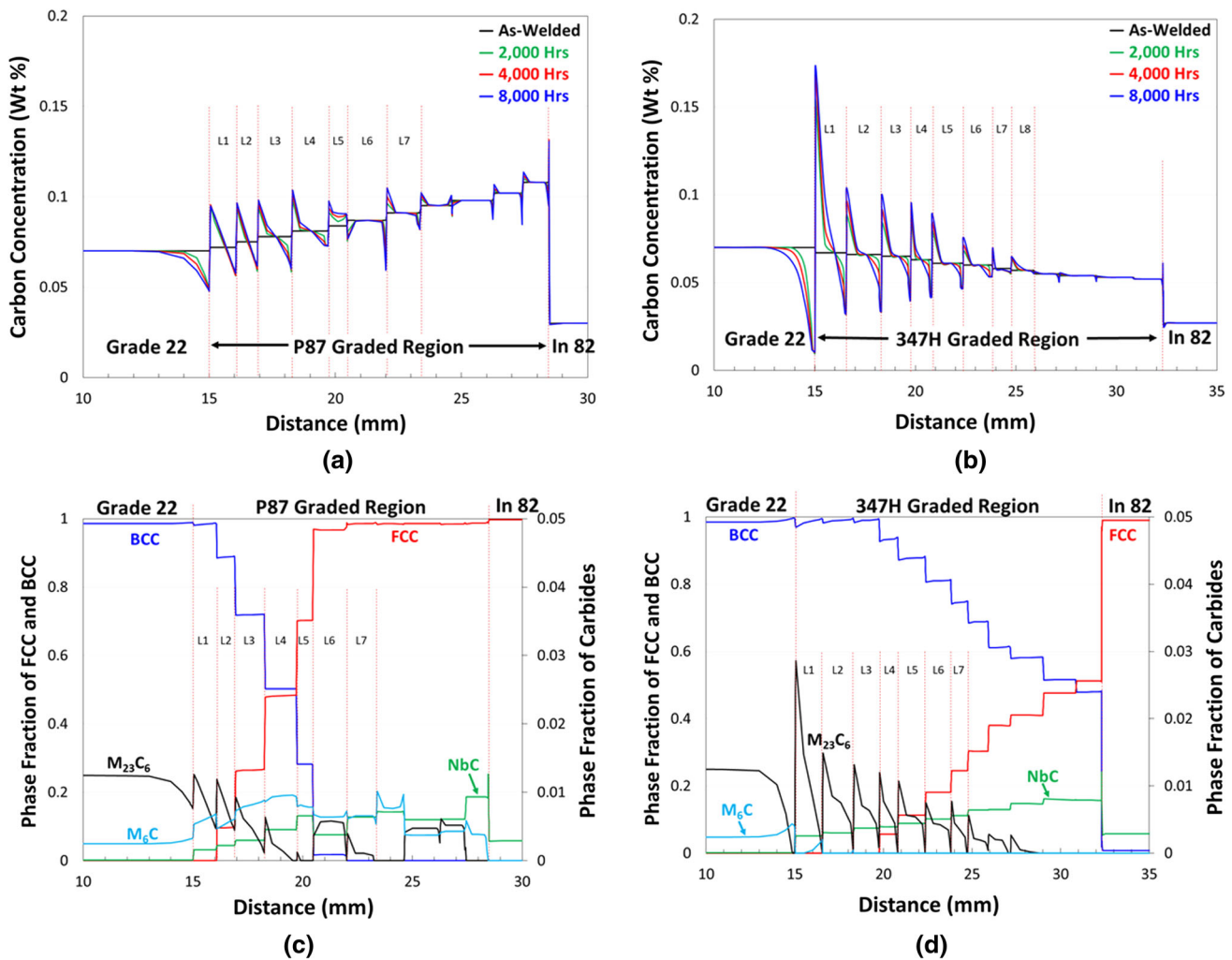


Fig. 5—The carbon concentration and phase fraction as a function of distance at the simulated aging temperature of 600 °C for 8000 h for (a, b) the P87 GTJ and (c, d) the 347H GTJ.

C. Microstructure Characterization

Photomicrographs were acquired in the Inconel 82 GTJ aged for 4000 hours at locations of significant microstructural evolution seen from the hardness and modeling results, and shown in Figure 7. The HAZ is directly adjacent to the interface, and the beginning of L1 is shown in Figures 7(a) and (b), respectively. The HAZ was originally martensitic in the as-welded condition. Upon aging, carbon diffusion resulted in a microstructure depleted of carbides, as shown in Figure 7(a). The microstructure in L1 adjacent to the HAZ/L1 interfaces is comprised of fine lath martensite populated by carbides, which were determined to be Cr rich. Figure 7(c) shows a microstructure at the end of L1 that is somewhat similar to Figure 7, however, the population of carbides is reduced and a coarser, lath martensite is observed. Finally, the microstructure in L2 (Figure 7(d)) shows an increase in carbide content, and the formation of a secondary constituent. Identical microstructural trends were observed in GTJs made with P87 and 347H filler metal.

Figures 8(a) and (b) show EBSD phase maps overlaid with image quality maps of the layer interfaces where the BCC/FCC transition occurs in GTJs using Inconel 82 and P87, respectively. (EBSD results shown here do not differentiate between BCC ferrite, BCC bainite, and BCT martensite. Thus, for simplicity, the phase map is shown for BCC ferrite and FCC austenite.) All samples were examined in the 2000-hour aged condition.

The phase maps are shown for the L4/L5 and L5/L6 interfaces for the Inconel 82 GTJ. Layer 4 consists of all BCC, and L5 shows the initial formation of austenite. Beyond the L5/L6 interface, only FCC is stable. Similar results are shown in Figure 8(b) for the P87 GTJ, except the interfaces between L6/L7 and L7/L8 were investigated. Layer 7 represents the region of mixed BCC/FCC, with L8 consisting of all FCC. Figure 8(c) represents four regions throughout the 347H GTJ where the martensite/austenite transition occurs. Layer 9 consists of all BCC, and L10 has a small amount of FCC in a BCC matrix. Layers 11 and 12 exhibit increasing amounts of the FCC phase. Beyond L12,

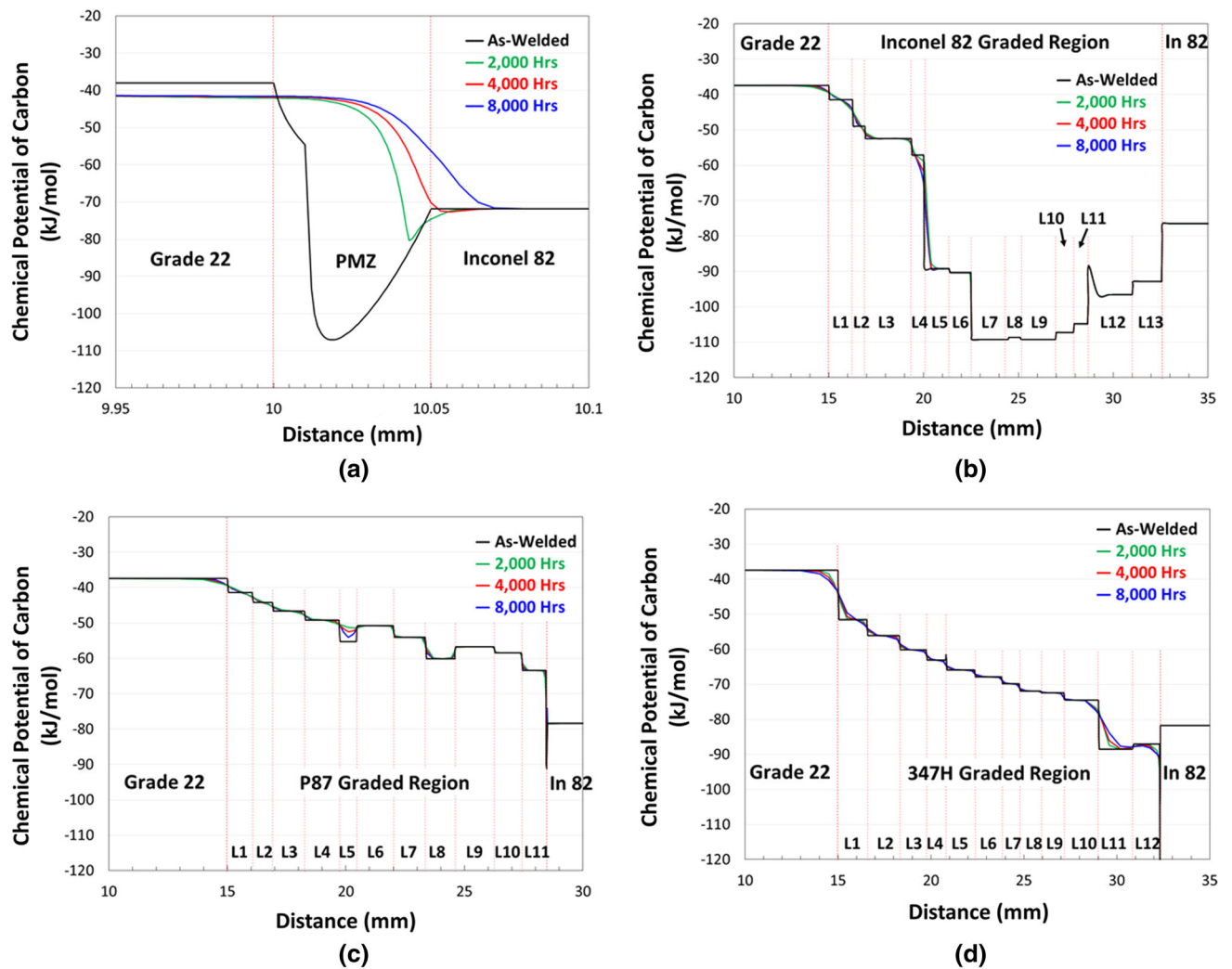


Fig. 6—The chemical potential of carbon at 600 °C in the as-welded and aged conditions for (a) conventional DMW, (b) Inconel 82 GTJ, (c) P87 GTJ, and (d) 347H GTJ.

Inconel 82 was joined to the 800H extension and exhibited all FCC (as confirmed with EBSD).

Layer 7 in the as-welded P87 GTJ was analyzed to understand the cause for the mixed BCC/FCC microstructure. Figure 9(a) shows a light optical image superimposed on an SEM photomicrograph of L7 with hardness indents used as markers for regions of interest. The dark and light regions, representing cell core and intercellular regions, correspond to the BCC and FCC austenite phases, respectively. Additionally, an EDS line scan (shown by the black arrow in Figure 9(a)) was conducted across the region to understand the elemental distribution that could be attributed to the stability of the FCC phase. The results of the EDS line scan are presented in Figure 9(b) showing Fe, Cr, Ni, C, and Mo (other elements were analyzed but not included). The analysis of carbon was calculated by considering a constant carbon concentration of L7 (0.091 wt pct). Next, the EDS trace was subjected to a simulated weld thermal cycle from DICTRA. Due to the alloying element segregation and corresponding CPC gradient, the carbon will diffuse to the cell core, as shown in

Figure 9(b). The trace initiated in an intercellular region is depleted in Fe, and enriched in the remaining measured elements. Conversely, the cell core is enriched in Fe and depleted in the remaining elements. Figures 9(c) and (d) show results from the solidification simulation for this layer composition. For this composition profile shown in Figure 9(d), the cell core is the initial solidification region (far left on figure), with the intercellular region solidifying last. The calculated distribution of the elements shown is in good agreement with the measured elements, as Fe is depleted in the intercellular region when the other elements become enriched.

D. Evaluation of Ni-Rich Constituent

Briefly mentioned above (in Figure 7(d)) was the formation of a secondary constituent observed in all three GTJs. An example of this is shown in Figures 10(a) through (d) that represents L2 through L5 in the P87 GTJ aged for 8000 hours, respectively. The constituent is in the form of elongated particles in

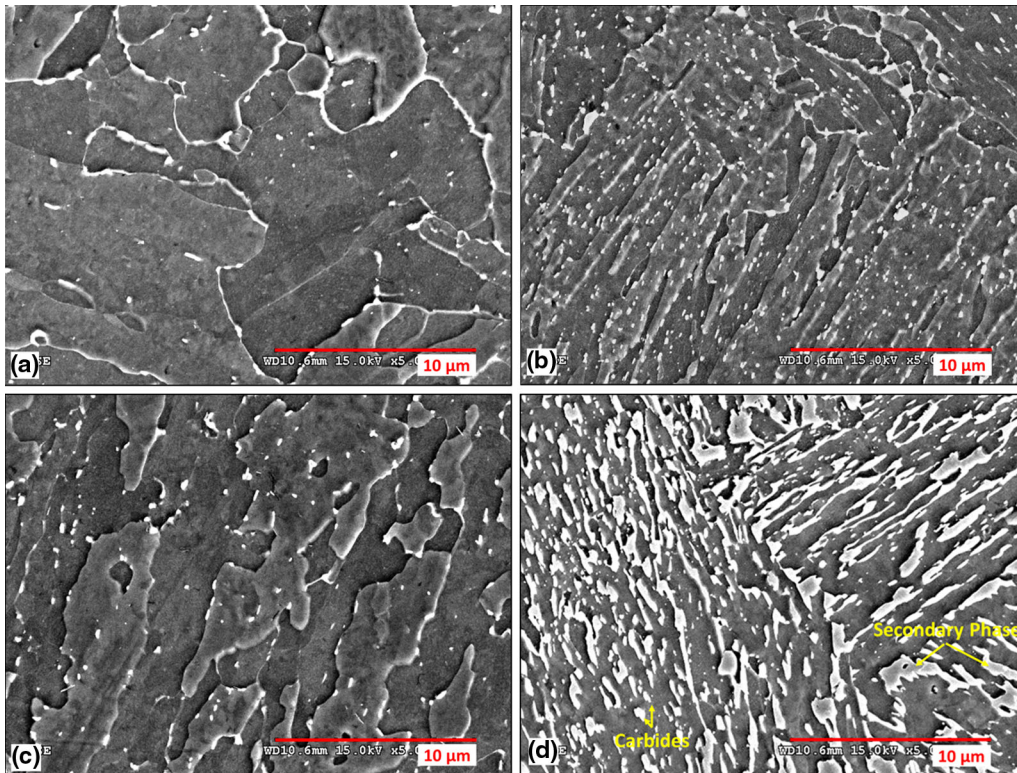


Fig. 7—SEM photomicrographs of the Inconel 82 GTJ aged for 4000 h showing (a) Grade 22 substrate HAZ, (b) beginning of L1, (c) end of L1, and (d) beginning of L2.

L2 and L3 (Figures 10(a) and (b)) that increases in volume fraction with increasing layer. The calculated phase fraction as a function of temperature for the P87 GTJ is shown in Figures 11(a) through (d) for L2 to L4, respectively. Paying specific attention to 600 °C, the austenite that forms during aging increases in phase fraction with increasing layer, going from 12 percent FCC in L2 (Figure 11(a)) to 76 percent FCC in L5 (Figure 11(d)). The austenite that exists at 600 °C will also transform to martensite without a change in composition when cooled to T_{RM} , thus accounting for the presence of this martensite constituent within the GTJs after aging.^[33] Also labeled on the plots are the “Ac3” temperatures, which are designated as the location where BCC completely dissolves upon heating. As shown, increasing layers exhibit progressively lower Ac3 temperatures, ranging from 734 °C in L2 (Figure 11(a)) to 625 °C in L5 (Figure 11(d)). It must be recognized that these are under equilibrium conditions. The heating rates experienced during welding are significantly faster than equilibrium and therefore, it is expected for these temperatures to be higher.^[34] Additionally, the accuracy of Thermo-Calc at lower temperatures is limited due to the insufficient low temperature data available from the databases used for the models. Thus, the trends are more important than the actual Ac3 values. This will be discussed further in the next section. Figure 12(a) shows the calculated composition of the FCC phase at 600 °C directly compared to the measured composition of the martensite constituent. This constituent is Ni rich at T_{RM} and is in very good agreement with the

calculated composition of the austenite phase at 600 °C. Similarly, Figure 12(b) shows very good agreement between the measured matrix and calculated BCC phase compositions.

The morphology of the Ni-rich martensite was different between filler metals. This is shown in Figure 13 where the Ni-rich martensite is observed in the 347H GTJ. The Ni-rich martensite has a different morphology than that observed in the GTJs using Inconel 82 and P87 (see Figures 7(d) and 10(b) for comparison). The martensite morphology in Inconel 82 and P87 GTJs is rod-like, whereas the martensite in the 347H GTJ exhibits a blocky morphology.

IV. DISCUSSION

A. As-Welded Microstructures

The analysis of the as-welded microstructures is summarized in Figure 2 with the combination of hardness, composition, and M_s temperature. The conventional DMW (Figure 2(a)) shows a high hardness in the HAZ. This is attributed to martensite formation during fabrication from the high cooling rates associated with welding. Directly after the HAZ, the GTJs exhibit increased hardness with each layer (*i.e.*, before the fully austenitic region is reached). This hardness variation is associated with several factors that are all related to the variation in composition, including changes in both the M_s and Ac3 temperatures, along with solid solution

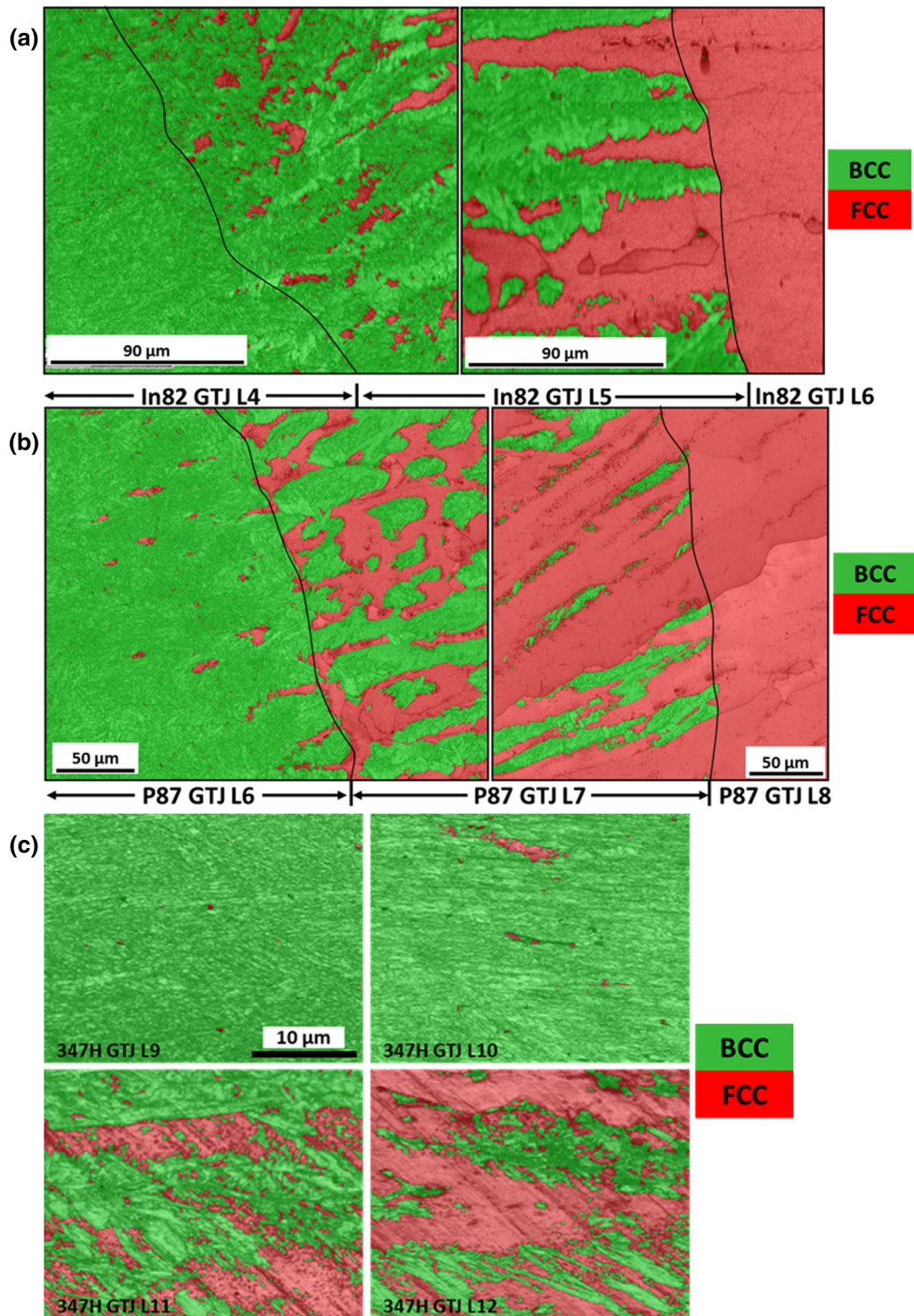
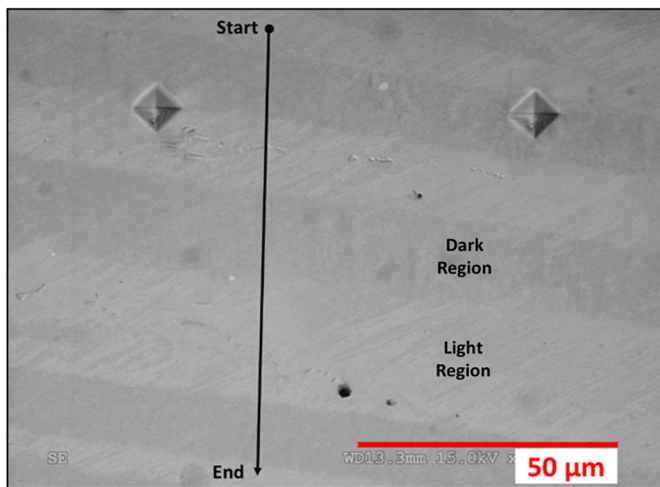


Fig. 8—EBSD phase maps overlaid with image quality maps showing the transition to austenite for the GTJ using (a) Inconel 82, (b) P87, and (c) 347H. (Note micron bar in L9 is for all four layers).

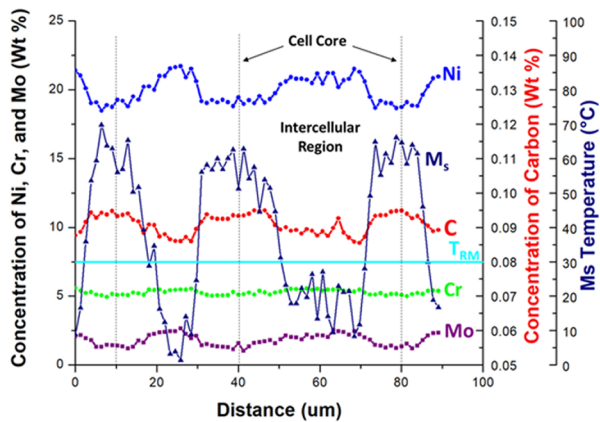
strengthening. The increase in alloying elements along the grade suppresses the M_s temperature (Figures 2(b) through (d)). If martensite forms at an elevated temperature (*i.e.*, the M_s temperature is relatively high), then significant auto-tempering can occur during cooling to T_{RM} . Therefore, the layers with higher M_s temperatures will experience a larger degree of auto-tempering, thus

lowering the hardness. This explains, in part, the lower hardness values observed near the beginning of the grade where the M_s temperature is relatively high.

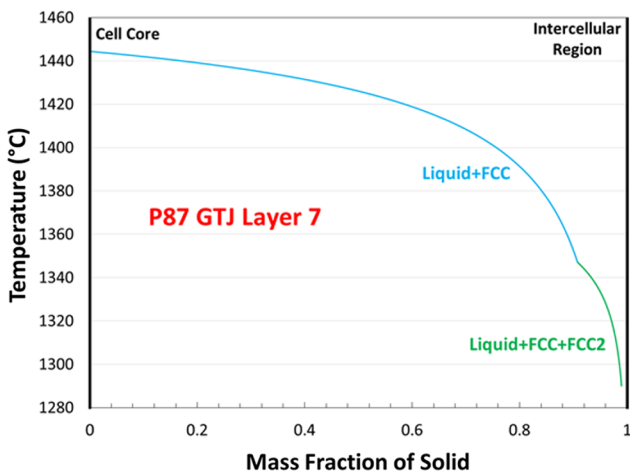
As demonstrated in Figure 11, the Ac_3 temperature will also decrease with each additional layer within the graded region (due to the increased alloy content). The relatively high alloy content within the layers provides



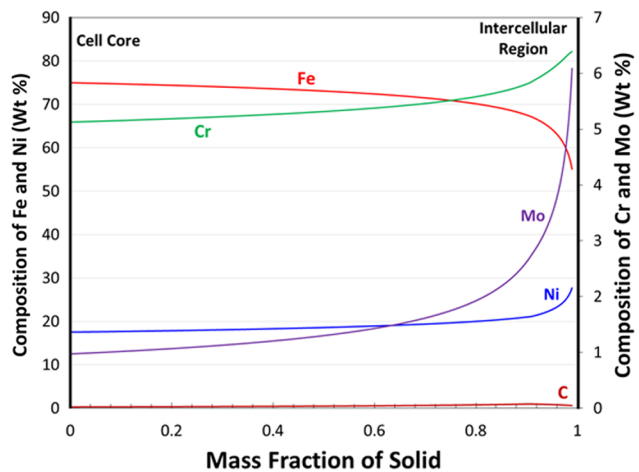
(a)



(b)



(c)



(d)

Fig. 9—(a) LOM image superimposed over the SEM image showing the location of the EDS scan in L7 of the P87 GTJ, (b) the results from the EDS scan with the M_s temperature, (c) Scheil solidification simulation of L7 showing the phases that form, and (d) element distribution of L7 in FCC during solidification.

high hardenability that, combined with the fast cooling rates from welding, will produce martensite during cooling for any region heated above the Ac_3 temperature. Since the Ac_3 temperature decreases along the graded region, the amount of material exposed to peak temperatures above Ac_3 increases with each additional layer, thus leading to more as-quenched martensite. This effect also partly accounts for the increased hardness along the length of the grade. The increased hardness in the first several layers can also partly be attributed to solid solution strengthening, as it is known that Ni and Cr increase the strength of martensite.^[35–37]

After the initial increase in hardness within the first several layers of the graded regions in the GTJs, there is a significant hardness decrease (at locations of $x = 15$, 19, and 24 mm for Inconel 82, P87 and 347H GTJs, respectively). Figure 8 shows that this hardness reduction is associated with austenite formation. The austenite phase stability can primarily be attributed to the

increase in Ni concentration along the grade that eventually drives the M_s temperature below T_{RM} , thus stabilizing austenite. Formation of the mixed martensite/austenite regions can be understood with reference to solidification simulations, shown in Figure 9. Austenite (FCC) and carbides form during solidification (Figure 9(c)), and the segregation of the alloying elements plays a major role in the microstructure that forms upon cooling to T_{RM} . Cr, Ni, and Mo segregate to the intercellular regions (light regions in Figure 9(a)). Equation [2] can be used to estimate the variation in M_s temperature with position along the cellular substructure due to the microsegregation. The M_s temperature varies above and below T_{RM} (shown by the blue horizontal line) in the cell core and intercellular regions, respectively. This is consistent with the phases present from EBSD analysis in L7 of the P87 GTJ where austenite is stable in the intercellular regions, which is attributed to the M_s temperature suppressed below T_{RM} .

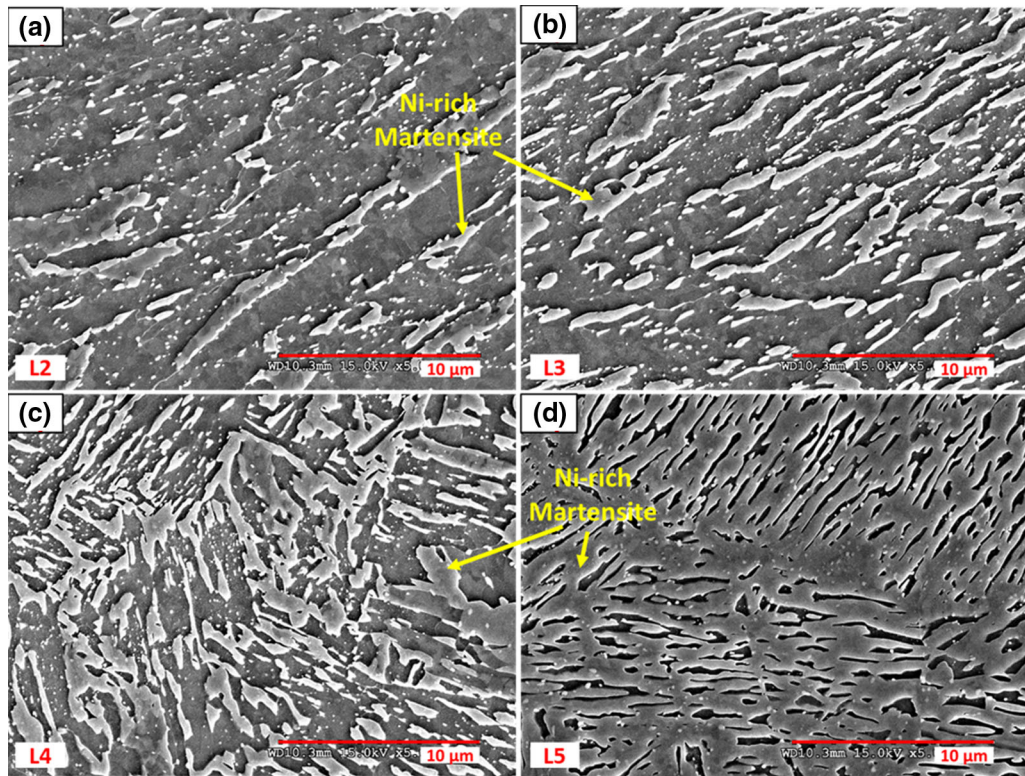


Fig. 10—SEM photomicrographs of the P87 GTJ aged for 8000 h showing the extent of the Ni-rich martensite formation for (a) L2, (b) L3, (c) L4, and (d) L5.

V. SIMULATED RESULTS

Some of the simulation results provide particular insight into microstructural evolution during aging (discussed below). Note that the $M_{23}C_6$ carbide stability follows the carbon concentration profiles (Figures 4(c) and (d) for Inconel 82, Figures 5(a) and (b) for P87, and Figures 5(c) and (d) for 347H). The carbon concentration depletes prior to every interface, and enriches into the subsequent layer. This is controlled by the CPC gradient (Figure 6), as carbon will diffuse down the gradient to alleviate the CPC discontinuity at the interface. Nearly all the carbon resides in carbides.^[16] Therefore, carbon must dissolve into the matrix in order to diffuse. Of the three carbides in the system ($M_{23}C_6$, M_6C , and NbC), the $M_{23}C_6$ carbide is the least stable. $M_{23}C_6$ is considered a low temperature carbide due to its complex structure and lower dissolution temperature, which is confirmed in the equilibrium calculations shown in Figure 11.^[34] For these reasons, this carbide will dissolve before the M_6C and NbC carbides.

In the Inconel 82 GTJ, there is negligible diffusion at the layer interfaces after L4 (Figure 4(c)), which is coincident with the $M_{23}C_6$ carbide dissolution and NbC stability (Figure 4(d)). Additionally, austenite becomes the dominant phase in this region. Carbon can diffuse faster through BCC, thus the FCC matrix after L4 limits the diffusion of carbon in the matrix.^[38] Furthermore, the carbon resides in the Nb carbide (since the $M_{23}C_6$ carbide dissolved), which also shows negligible enrichment or depletion at the layer interfaces. Even though

chromium is relatively high in Inconel 82, the increase in Nb concentration across the graded region stabilizes NbC over the $M_{23}C_6$ carbide at 600 °C. It is interesting to note that even the sharp discontinuities in CPC at the interfaces are not alleviated after aging up to 8000 hours. This effect may be associated with carbon being tied up in the highly stable NbC. Similar trends are shown in the other two filler metals.

A. Aged Microstructures

The modeling results described above can be combined with experimental observations to explain the hardness trends observed in Figures 3(a) through (d). The conventional DMW exhibits a reduction in hardness in the HAZ that is attributed to tempering of the martensitic microstructure during aging. Additionally, there is a localized reduction in hardness directly adjacent to the fusion line that can be attributed to carbon diffusion, which results in a carbon-depleted region in the HAZ of Grade 22, and a carbon-enriched region in the PMZ. This is consistent with the carbon diffusion calculation (Figure 4(a)) that shows the same carbon-depleted and carbon-enriched regions in the HAZ and PMZ, respectively. The carbon diffusion is attributed to the negative chemical potential gradient from the Grade 22 to the Inconel 82. Carbon will eventually exceed the solubility limit in the PMZ, resulting in $M_{23}C_6$ formation, as shown in the phase fraction of carbides in Figure 4(b). A local increase in

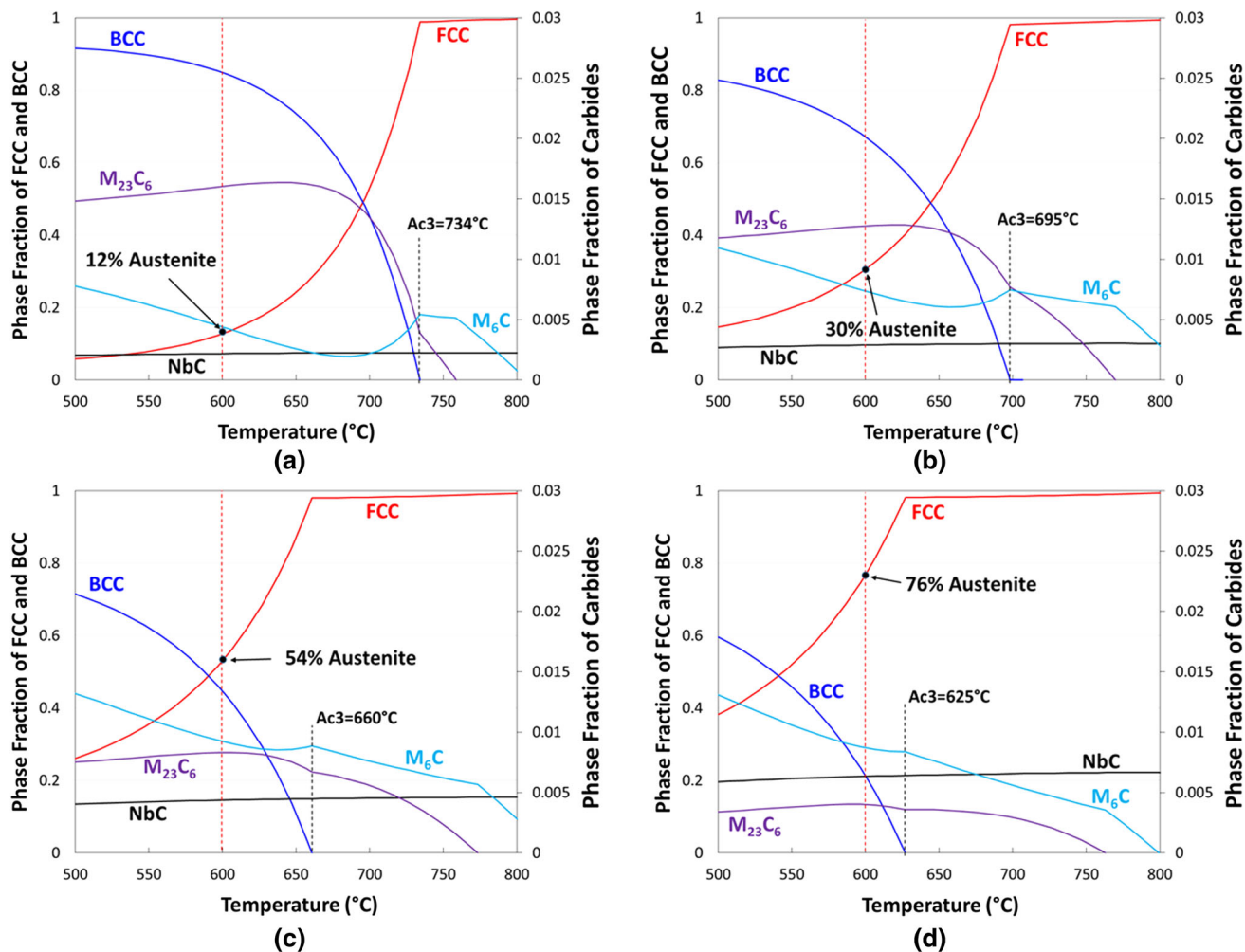


Fig. 11—Calculated phase fraction as a function of temperatures for in (a) L2, (b) L3, (c) L4, and (d) L5 for the P87 GTJ for a simulated age at 600 °C.

carbide content will increase the hardness, and this is consistent with the hardness trace shown in Figure 3(a).

The GTJs experience the same trend as the DMW regarding the tempering of the martensitic microstructure in the HAZ, which contributes to the observed reduction in hardness. Additionally, there is an overall reduction in hardness in the martensitic layers of the graded region for all three filler metals, prior to the austenite formation. This is also attributed to the tempering of the martensitic microstructure during aging. Furthermore, enhanced carbon diffusion occurs in the GTJs at the layer interfaces, as shown in Figures 4(c) and 5((a) and (c)). This is consistent with the photomicrographs in Figure 7 that show the carbides in the regions of significant hardness changes in the beginning layers, specifically in the Inconel 82 GTJ. All three filler metals exhibit a hardness decrease in the HAZ adjacent to the HAZ/L1 interface, and an increase at the beginning of L1. The carbon (and corresponding carbide) calculation also exhibits depletion and enrichment in these regions, shown by the calculated carbon and $M_{23}C_6$ carbide in Figures 4(c) and (d). The

microstructural features in these images presented in Figure 7 are consistent with the $M_{23}C_6$ carbide trend, and account for the hardness decrease in the HAZ, and the increase into L1 (Figure 3(b)). Additionally, a decrease in hardness across L1 is shown for Inconel 82 and P87 in all aged conditions, and observed in 347H after 8000 hours. This can also be attributed to variation in $M_{23}C_6$ content shown in the model, and validated by the observations in the photomicrographs represented by the Inconel 82 GTJ in Figures 7(b) and (c). In addition, the lath martensite is relatively fine in the beginning of L1 and coarser at the end of L1, which can also contribute to the hardness decrease across this layer. The combination of reduced carbides and coarser lath martensite accounts for the observed decrease in hardness across the layer. As described previously, although carbon diffusion and the associated microstructural changes are somewhat accelerated near the interfaces of the GTJs, they are significantly reduced relative to the conventional DMW. The P87 GTJ exhibits similar trends. In this case, L6 exhibits decreased hardness (relative to L5) that is associated with a mixed martensite/austenite structure.

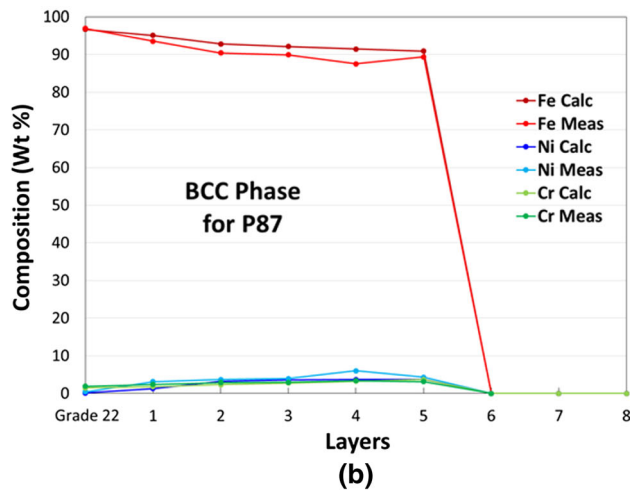
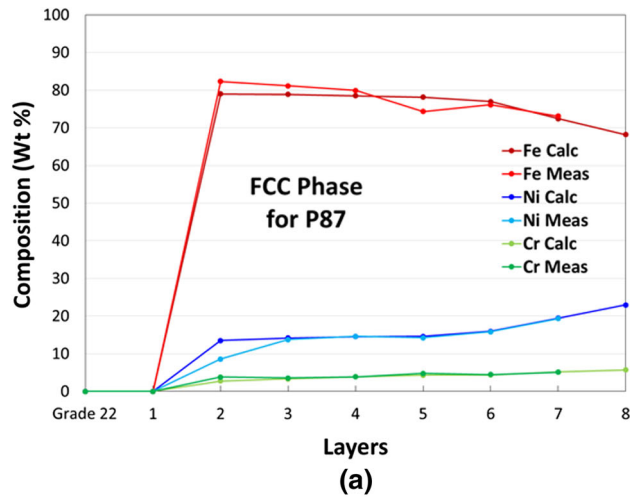


Fig. 12—The measured and calculated compositions as a function of layers for (a) FCC phase and (b) BCC phase in the P87 GTJ.

The increase in hardness observed in the Inconel 82 GTJ after 8000 hours and the 347H GTJ after L10 after aging for 2000 hours can likely be attributed to precipitation that is known to occur in these alloys. Alloy 347H forms Nb carbides during aging.^[39–44] Hajiannia *et al.*^[39] revealed that fine intercellular Nb carbide precipitates increased the hardness of the welded 347H after aging. This is consistent with the results of Minami *et al.*^[41] who used transmission electron microscopy to show the presence of fine nanometer scale Nb carbides in the same alloy. The presence of the fine Nb carbides also contributes to the increase in hardness in the Inconel 82 GTJ. Klueh and King^[45] investigated the thermal aging behavior of Inconel 82 after aging up to 10,000 hours at various temperatures. They also observed a precipitate that developed in the matrix that was associated with the cellular–dendritic substructure and the concomitant solute rejection from the solidification process. Since Inconel 82 has a Nb content of 2.36 wt pct, it is expected Nb carbides will form and provide an overall increase in strength. The presence of Nb carbides in both materials is consistent with the calculated carbide phase fraction from the simulations that show the stability of NbC in the graded region.

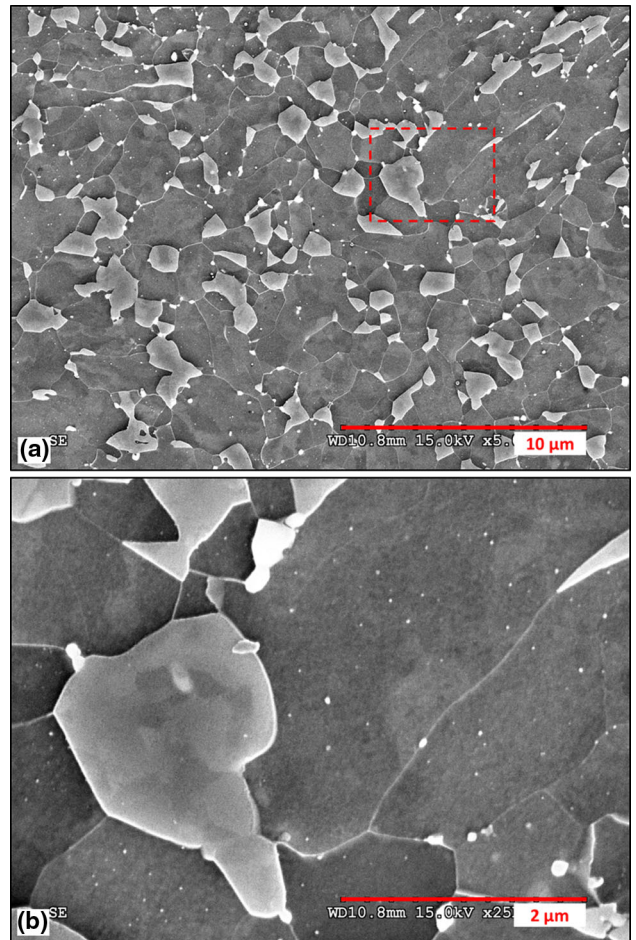


Fig. 13—SEM photomicrograph of L6 in the 347H GTJ aged for 8000 h showing the Ni-rich martensite for (a) low and (b) high magnifications.

B. Ni-Rich Martensite

The Ni-rich martensite does not form in the as-welded condition, but forms in all the GTJs after aging at 600 °C due to austenite stability at this temperature. Austenite stability was confirmed in Figure 11 that shows thermodynamic equilibrium plots for a given layer. With increasing layer, the amount of FCC phase increases and, upon cooling, transforms to martensite. This is confirmed with the photomicrographs in Figure 10. Since the martensite transformation is diffusionless, the as-quenched martensite has the same composition of the parent austenite, most notably Ni.^[33] This is confirmed with EDS results showing that the martensite is rich in Ni for the FCC phase (Figure 12(a)) as compared to the Ni in the BCC phase (Figure 12(b)). This is also confirmed from the EBSD results that show BCC is the stable phase until L7 (P87 GTJ), L5 (Inconel 82 GTJ), and L10 (347H GTJ). The lack of Ni-rich martensite in the as-welded condition is associated with the time necessary for austenite formation at 600 °C. Figure 14(a) provides simulation results for non-equilibrium solidification of L3 for the Inconel 82 GTJ that shows FCC and carbides are expected to form during solidification. Due to the high cooling rates

from the weld thermal cycles (and the high hardenability of this layer), the austenite transforms to martensite during cooling. The subsequent thermal cycles do not allow enough time for the FCC phase to form at an elevated temperature. This is demonstrated in Figure 14(b) that shows the phase fraction as a function of time, aging from 400 to 600 °C. Since low temperature kinetic data are limited, the Inconel 82 GTJ L3 (as an example) was simulated at a temperature of 400 °C and then heated to 600 °C. It takes almost 20 hours for the BCC and FCC phases to stabilize to the 600 °C equilibrium phase fraction values. The sluggish transformation kinetics can be attributed to the low diffusivity of Ni in austenite. The inability to form Ni-rich austenite during the short thermal cycles associated with welding accounts for the lack of Ni-rich martensite in the as-welded condition.

Although the hardness and amount of Ni-rich martensite each increase along the grade, the increase in hardness cannot be attributed to the presence of the

Ni-rich martensite. The hardness of martensite is largely affected by carbon concentration. The Ni-rich martensite could potentially have relatively high carbon (due to the high solubility of carbon in austenite). However, under these conditions, nearly all the carbon is tied up in the carbides.^[16] This is confirmed from thermodynamic calculations, which demonstrate that the carbon in the FCC and BCC phases at 600 °C was less than 1×10^{-5} wt pct carbon, and the rest of the carbon was in the carbides. Additionally, nanohardness measurements conducted on each phase showed that the BCC matrix hardness was 4.84 ± 0.77 GPa, while the Ni-rich martensite had a hardness of 5.06 ± 0.43 GPa. Thus, there is no significant difference in hardness between these two phases. Finally, note that the hardness increases along the grade in the as-welded condition when no Ni-rich martensite is present, which is also consistent with the above observation.

The formation of a similar Ni-rich martensite has been reported in other studies.^[46–49] The martensite morphology is largely effected by the initial microstructure prior to aging. When the sample is heated to 600 °C, there will be regions where this temperature is above the A_{c1} temperature (defined as the initiation of austenite transformation upon heating) and thus, austenite is stable. The initiation sites for the parent austenite formation are the martensite laths or prior austenite grain boundaries (PAGB).^[46,47,50,51] The austenite that forms at the PAGB and/or lath boundaries will transform to a Ni-rich martensite, and take the form of rod-like morphology or blocky morphology, also described in the literature as “islands.”^[52] The blocky Ni-rich martensite forms mostly at the PAGB, while the rod-like martensite forms on the martensite laths.^[50,51,53] A blocky morphology is clearly observed in Figure 13 for the 347H GTJ. Conversely, the elongated morphology of the Ni-rich martensite can be seen in Figures 7(d) and 10(b) for Inconel 82 and P87, respectively.

Work is in progress to understand the tensile and creep properties of these GTJs relative to conventional DMWs and will be reported in separate articles.

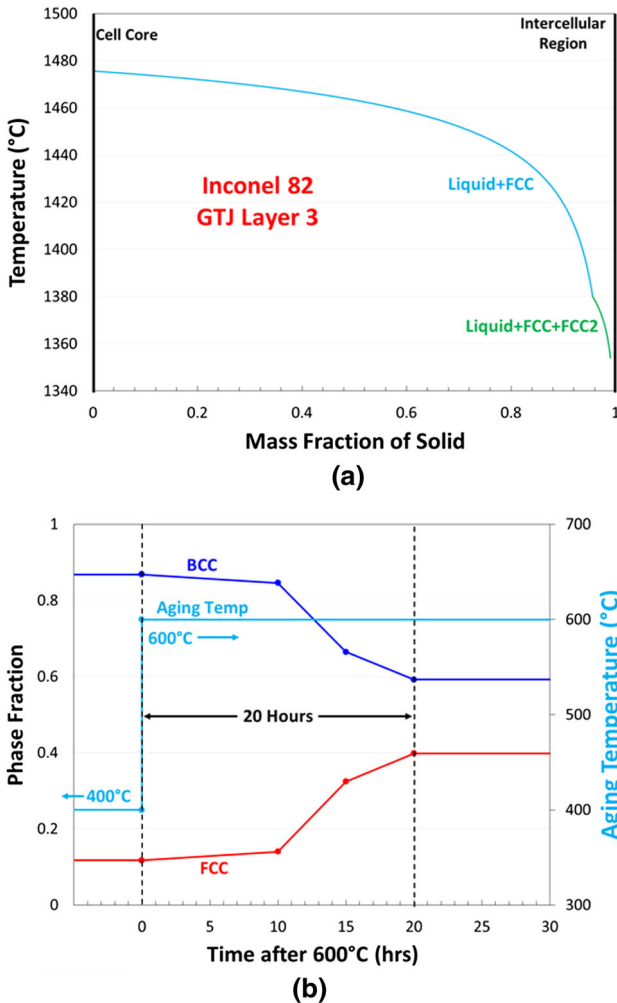


Fig. 14—(a) Scheil solidification model for the Inconel 82 GTJ L3 showing the phases that form upon solidification, and (b) phase fraction and aging temperature as a function of time after reaching 600 °C that shows how long it takes for the BCC and FCC phases to stabilize in L3 of the Inconel 82 GTJ.

VI. CONCLUSIONS

Microstructural characterization was conducted on three GTJs in the as-welded and aged conditions. Thermodynamic and kinetic modeling of the joints was compared to the experimental results. The following conclusions can be drawn from this work.

1. The graded regions of the GTJs in the as-welded condition exhibit martensite in the first few layers of the grade, followed by a mixed martensite/austenite region, and then a fully austenitic region in the final layers.
2. The austenite stability in the final layers is attributed to the increase in Ni concentration that reduces the martensite start temperature below room temperature, thus stabilizing austenite. The preceding layers of mixed FCC/BCC are attributed to element segregation upon solidification that

- causes the martensite start temperature to vary above and below room temperature.
- The increase in hardness within the martensitic region of the grade in the as-welded condition is associated with a decrease in the M_s temperature (less auto-tempering), a decrease in the Ac3 temperature (more as-quenched martensite), and solid solution strengthening. The subsequent decrease in hardness is associated with the austenite stability in the final layers.
 - Enhanced carbon diffusion occurs at the layer interfaces during aging, and is more significant in the beginning layers of the graded region. Although the carbon is tied up in carbides, the $M_{23}C_6$ carbide will dissolve, allowing carbon to diffuse due to the chemical potential gradient that is steepest in the beginning of the grade.
 - Hardness gradients between the layers can be attributed to the distribution of carbides throughout the layers. Carbon/carbide-depleted and carbon-enriched regions form at the end and beginning of a layer, respectively. This coincides with the hardness variation, as the overall hardness was observed to be higher at the beginning of each layer.
 - During aging at 600 °C, both FCC and BCC phases are stable in the first several layers of the grade. The amount of Ni-rich FCC (austenite) increases as the Ni concentration increases throughout the grade. The Ni-rich austenite transforms to martensite with no change in composition during cooling.

REFERENCES

- G. Çam and M. Koçak: *Int. Mater. Rev.*, 1998, vol. 43, pp. 1–44.
- G. Çam and M. Koçak: *Sci. Technol. Weld. Join.*, 1998, vol. 3, pp. 159–75.
- G. Çam and G. Ipekoglu: *Int. J. Adv. Manuf. Technol.*, 2017, vol. 91, pp. 1851–66.
- R.L. Klueh and J.F. King: *Weld. J.*, 1982, vol. 62, pp. 302–11.
- J.N. DuPont: *Int. Mater. Rev.*, 2012, vol. 57, pp. 208–34.
- R. Dooley and P. Chang: *Proc. Int. Conf. on Boiler tube failures in fossil plants*, 1997, pp. 2–10.
- I. Ramu and S.C. Mohanty: *Procedia Mater. Sci.*, 2014, vol. 6, pp. 460–67.
- M. Bhandari and K. Purohit: *IOSR J. Mech. Civ. Eng.*, 2014, vol. 10, pp. 46–55.
- A. Gupta and M. Talha: *Prog. Aerosp. Sci.*, 2015, vol. 79, pp. 1–14.
- C.D. Lundin: *Weld. J.*, 1982, vol. 61, pp. 58–63.
- M. Gittos and T. Gooch: *Weld. Res. Suppl.*, 1992, vol. 71, pp. 461–72.
- G.J. Brentrup and J.N. DuPont: *Weld. J.*, 2013, vol. 92, pp. 72–79.
- G.J. Brentrup, B.S. Snowden, J.N. DuPont, and J.L. Grenstedt: *Weld. J.*, 2012, vol. 91, pp. 252–59.
- N. Sridharan, E. Cakmak, B. Jordan, D. Leonard, W.H. Peter, R.R. Dehoff, D. Gandy, and S.S. Babu: *Weld. J.*, 2017, vol. 96, pp. 295–306.
- J.N. Dupont and A.R. Marder: *Metall. Mater. Trans. B*, 1996, vol. 27B, pp. 481–89.
- J.P. Galler, J.N. Dupont, S.S. Babu, and M. Subramanian: *Metall. Mater. Trans. A*, 2018.
- D. Drouin, A.R. Couture, D. Joly, X. Tastet, and V. Aimez: *R. Gauvin*, 2007, vol. 29, pp. 92–101.
- A. Borgenstam, L. Höglund, J. Ågren, and A. Engström: *J. Phase Equilibria*, 2000, vol. 21, pp. 269–80.
- Thermo-Calc Software MOB2 TCS Alloy Mobility Database.
- Thermo-Calc Software TCFe7-TCS Steels/Fe-Alloys Database version 7.
- Thermo-Calc Software Ni-Data-v7 Ni-Alloys Database.
- R.L. Klueh: *Metall. Trans. A*, 1978, vol. 9, pp. 1591–98.
- K. Laha, K.S. Chandravathi, K.B.S. Rao, S.L. Mannan, and D.H. Sastry: *Metall. Mater. Trans. a*, 2001, vol. 32A, pp. 115–24.
- J.D. Parker and G.C. Stratford: *J. Mater. Sci.*, 2000, vol. 35, pp. 4099–107.
- Y. Zhou, Y. Li, Y. Liu, Q. Guo, C. Liu, L. Yu, C. Li, and H. Li: *J. Mater. Res.*, 2015, vol. 30, pp. 3642–52.
- S.W. Banovic, J.N. Dupont, and A.R. Marder: *Weld. J.*, 2001, vol. 80, pp. 63–70.
- J.N. Dupont and C.S. Kusko: *Weld. J.*, 2007, vol. 86, pp. 51s–54s.
- K.W. Andrews: *J. Iron Steel Inst.*, 1965, vol. 203, pp. 721–27.
- R.J. Christoffel and M.R. Curran: *Weld. J.*, 1956, vol. 35, pp. 457–68.
- D.A. Porter, K.E. Easterling, and M.Y. Sherif: *Phase Transformations in Metals and Alloys*, Taylor and Francis Group, Routledge, 2009.
- L.S. Darken: *Metall. Mater. Trans. B*, 1948, vol. 41B, pp. 430–38.
- J.F. Eckel: *Weld. J.*, 1964, vol. 43, pp. 170–78.
- G. Krauss: *Steels: Processing, Structure, and Performance*, ASM International, 2015.
- K. Sindo: *Welding Metallurgy*, 2nd ed., Wiley, New York, 2003, pp. 822–32.
- G. Krauss: *Mater. Sci. Eng. A*, 1999, vols. 273–275, pp. 40–57.
- E.C. Bain: *Functions of the Alloying Elements in Steel*, American Society for Metals, 1939.
- R.W. Hertzberg, R.P. Vinci, and J.L. Hertzberg: *Deformation and Fracture Mechanics of Engineering Materials*, Wiley, Hoboken, 2013.
- W.D. Callister and D.G. Rethwisch: *Materials Science and Engineering: An Introduction*, Wiley, New York, 2007, vol. 94.
- I. Hajiannia, M. Shamanian, and M. Kasiri: *Mater. Des.*, 2013, vol. 50, pp. 566–73.
- B. Shalchi Amirkhiz, S. Xu, J. Liang, and C. Bibby: in: *36th Annu. CNS Conf.*
- Y. Minami, H. Kimura, and M. Tanimura: *J. Mater. Energy Syst.*, 1985, vol. 7, pp. 45–54.
- R. Mittal and B.S. Sidhu: *J. Mater. Process. Technol.*, 2015, vol. 220, pp. 76–86.
- T. Sourmail: *Mater. Sci. Technol.*, 2001, vol. 17, pp. 1–14.
- H. Tanaka, M. Murata, F. Abe, and K. Yagi: *Mater. Sci. Eng. A*, 1997, vols. 234–236, pp. 1049–52.
- R.L. Klueh and J.F. King: 1981, p. ORNL-5783.
- E.J. Barrick, D. Jain, J.N. DuPont, and D.N. Seidman: *Metall. Mater. Trans. A*, 2017, vol. 48A, pp. 5890–910.
- D. Isheim, A.H. Hunter, X.J. Zhang, and D.N. Seidman: *Metall. Mater. Trans. A*, 2013, vol. 44, pp. 3046–59.
- D. Jain, D. Isheim, X.J. Zhang, G. Ghosh, and D.N. Seidman: *Metall. Mater. Trans. A*, 2017, vol. 48A, pp. 3642–54.
- S.J. Wu, G.J. Sun, Q.S. Ma, Q.Y. Shen, and L. Xu: *J. Mater. Process. Technol.*, 2013, vol. 213, pp. 120–28.
- F. Matsuda, K. Ikeuchi, Y. Fukada, Y. Horii, H. Okada, T. Shiwaku, C. Shiga, and S. Suzuki: *Trans. JWRI*, 1995, vol. 24, pp. 1–24.
- Y. Li and T.N. Baker: *Mater. Sci. Technol.*, 2010, vol. 26, pp. 1029–40.
- C.L. Davis and J.E. King: *Mater. Sci. Technol.*, 1993, vol. 9, pp. 8–15.
- X. Li, X. Ma, S.V. Subramanian, C. Shang, and R.D.K. Misra: *Mater. Sci. Eng. A*, 2014, vol. 616, pp. 141–47.

Publisher's Note Springer Nature remains neutral with regard to jurisdictional claims in published maps and institutional affiliations.